Investigation of Ca insertion into α-MoO_3 nanoparticles for high capacity Ca-ion cathodes

*Sanghyeon Kim[†,‡], Liang Yin[‡,§], Seong-Min Bak[ǀ], Timothy T. Fister[†,‡], Haesun Park[‡,‖,Δ], Prakash Parajuli[‡,#], Jihyeon Gim[†], Zhenzhen Yang[†,‡], Robert F. Klie[‡,#], Peter Zapol[‡,‖], Yonghua Du[ǀ], Saul H. Lapidus[‡,§], and John T. Vaughey[†,‡]**

[†] Chemical Sciences and Engineering Division, Argonne National Laboratory, Lemont, IL, 60439, USA

[‡] Joint Center for Energy Storage Research, Argonne National Laboratory, Lemont, IL 60439, USA

[§] X-ray Science Division, Advanced Photon Source, Argonne National Laboratory, Lemont, IL 60439, USA

[ǀ] National Synchrotron Light Source II, Brookhaven National Laboratory, Upton, New York, 11973, USA

[‖] Materials Science Division, Argonne National Laboratory, Lemont, IL 60439, USA

[Δ] School of Integrative Engineering, Chung-Ang University, Seoul, 06974, Republic of Korea

[#] Department of Physics, University of Illinois at Chicago, Chicago, IL 60607, USA

Corresponding Author

* E-mail: vaughey@anl.gov

KEYWORDS: multivalent batteries, calcium-ion batteries, layered structure, oxides, cathode materials, nanomaterials

ABSTRACT

Calcium-ion batteries (CIBs) are a promising alternative to lithium-ion batteries (LIBs) due to the low redox potential of calcium metal and high abundance of calcium compounds. Due to its layered structure, α-MoO_3 is regarded as a promising cathode host lattice. While studies have reported that α-MoO_3 can reversibly intercalate Ca-ions, limited electrochemical activity has been noted and its reaction mechanism remains unclear. Here, we re-examine Ca insertion into α-MoO_3 nanoparticles with a goal to improve reaction kinetics and clarify the storage mechanism. The α-MoO_3 electrodes demonstrated a specific capacity of 165 mA h g^{-1} centered near 2.7 V vs. Ca^{2+}/Ca, stable long-term cycling, and good rate performance at room temperature. This work demonstrates that under the correct conditions, layered oxides can be a promising host material for CIBs and renews prospects for CIBs.

LIBs have been the dominant energy storage system for portable electronics, consumer goods, and electric vehicles for nearly 30 years.[1,2] However, concerns regarding the costs of isolating the needed lithium sources, safety issues, and new portable power applications have led to an active search for beyond lithium-ion technologies.[3,4] Among these chemistries, energy storage systems based on multivalent charge carriers have received considerable attention as they have higher theoretical energy densities than LIBs when used in conjunction with metal anodes.[3–5] Among the many multivalent battery systems (such as Al^{3+}, Ca^{2+}, Mg^{2+}, Zn^{2+}), CIBs are one of the most promising candidates due to low reduction potential of calcium (−2.87 V vs. standard hydrogen electrode), safety (no dendrite formation), and the high elemental abundance of calcium.[6,7] However, to date, a CIB cathode with high energy density and Coulombic efficiency has not been demonstrated. While a full cell CIB requires a working Ca metal anode, that advance was only recently demonstrated,[8–12] and the discovery of stable and high energy density calcium ion cathodes is still required to achieve practical energy density values for CIBs.

Orthorhombic α-MoO_3 is a compelling cathode candidate as it is a well-known intercalation host for monovalent and multivalent cations and has a stable layered structure known to intercalate a variety of guest ions.[13–25] Additionally highly ionic oxide frameworks typically enable higher cell voltages compared to those built using soft anions (i.e., S, Se)[26] while providing good structural stability during cycling. Ca-ion intercalation into α-MoO_3 was first reported in 2018[24,25] using micron-scale bulk and ball-milled particles. Although the delivered capacities were attributed to Ca intercalation, some major issues remain unsolved. They showed featureless discharge curves with no clear reaction voltage plateaus while exhibiting large voltage hysteresis with specific capacities not in line with the predicted theoretical capacity (186 mA h g^{-1} assuming 1 electron reaction; $Ca_{0.5}MoO_3$) at a reasonable current density. This may be related to sluggish Ca^{2+} diffusion within the lattice since the divalent charge of Ca^{2+} ion has a strong coulombic interaction with other ions in the framework, leading to high activation energy barrier. This reaction kinetic issue can be addressed by reducing the particle size by an order of magnitude to provide shorter Ca^{2+} diffusion pathways and increase the amount of the electrodes surface exposed to the electrolyte.[27,28] Previous studies suggest that ball milling may not be an ideal method to reduce particle size of bulk material because it can damage the structure of the material and affect its electrochemical performance negatively. Thus, better performance is expected when materials are synthesized directly. Also, as α-MoO_3 is a relatively cation agnostic host material, a more detailed characterization suite needs to be done to confirm Ca^{+2} intercalation. This is important to the beyond Li-ion field as co-intercalation of other ions or side reactions can occur that contribute to the observed reversible electrochemical reactions. Thus, it is significant to observe the necessary changes rather than claiming Ca intercalation based purely on electrochemical data. There has been only one report of using hydrated MoO_3 for Ca cathode.[29] Although it showed a high specific capacity at room temperature, lattice water in the host structure lowers volumetric energy density and could exchange with the electrolyte solvent, leading to side reactions, anode passivation, and salt degradation. Since the ability of a dehydrated α-MoO_3 to accommodate Ca^{2+} is still not fully understood, further mechanistic studies are required to understand the storage pathways and charge compensation mechanisms.

Here, we evaluated α-MoO_3 nanoparticles as CIB cathodes in order to address the issues associated with the extent of intercalation and the mechanism of insertion. In this study, it was found that a nanoscaled α-MoO_3 reversibly cycle Ca-ions in non-aqueous electrolyte at room temperature. The mechanism of electrochemical Ca insertion into α-MoO_3 nanoparticles was investigated using multimodal X-ray synchrotron techniques including high resolution X-ray diffraction (XRD), X-ray absorption spectroscopy (XAS), and X-ray fluorescence (XRF) imaging and density functional theory (DFT) calculations.

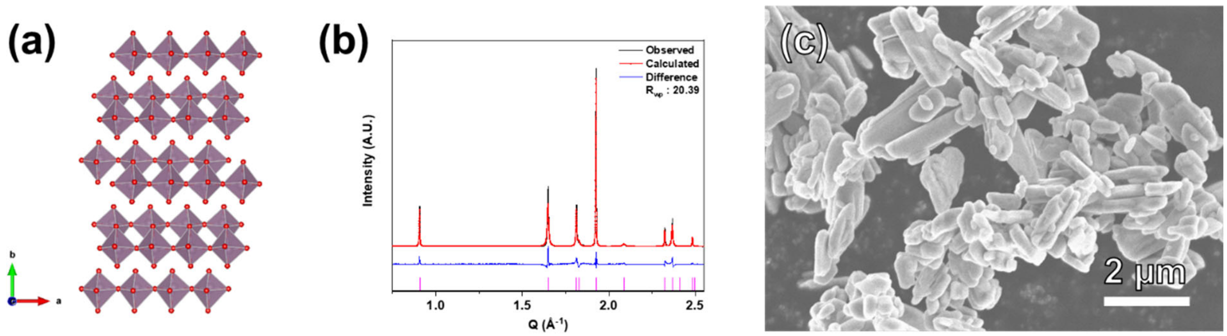

Figure 1. (a) Crystal structure, (b) Synchrotron XRD patterns and Rietveld refinement, (c) SEM image of α-MoO_3 nanoparticles.

Figure 1a shows the orthorhombic layered structure of α-MoO_3 consisting of two octahedral [MoO_6] layers joined by an edge (along the [100] direction) and corner (along the [001] direction). These planes are alternately stacked and separated by weak van der Waals attraction forces along the [010] direction where guest ions can be easily accommodated between the layers. The framework Mo^{+6} cations are reduced to balance the charges. Rietveld refinements of synchrotron diffraction data of the α-MoO_3 nanoparticles confirmed the space group of orthorhombic Pbnm (Figure 1b). The scanning electron microscope (SEM) image of α-MoO_3 nanoparticles (Figure 1c) shows irregular nanorod morphology with a width of 150 ~ 200 nm.

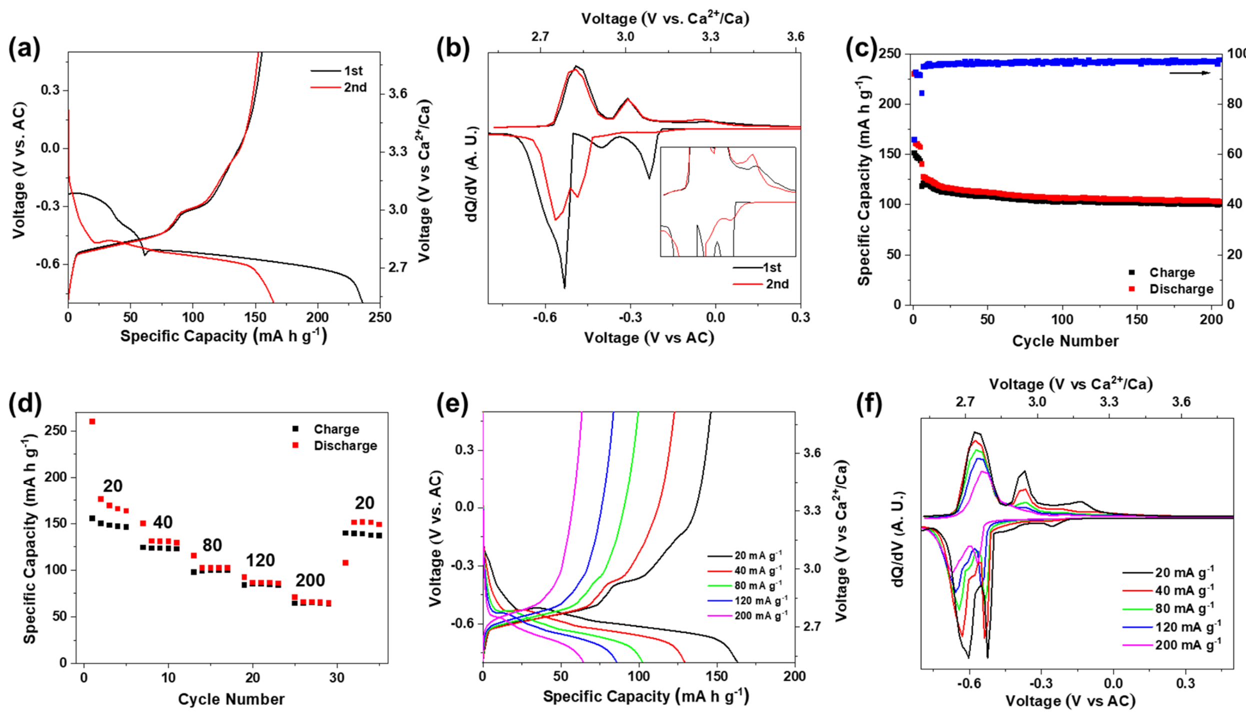

Figure 2. (a) 1st and 2nd cycle galvanostatic discharge-charge curves of α-MoO_3 nanoparticles at 20 mA h g^{-1} at room temperature. (b) Corresponding differential capacity plot for Fig 2a. The inset shows the magnified Fig. 2b (c) Cycling performance of α-MoO_3 nanoparticles at 40 mA g^{-1} after 5 cycles at 20 mA h g^{-1} at room temperature. (d) Rate performance of α-MoO_3 nanoparticles at different c-rates ranging from 20 mA g^{-1} to 200 mA g^{-1} at room temperature. (e) Galvanostatic discharge-charge curves of α-MoO_3 nanoparticles at different c-rates. (f) Corresponding differential capacity plot for Fig 2e.

The α-MoO_3 nanoparticle electrodes were examined as Ca-ion electrodes using galvanostatic discharge/charge tests. The capacitive AC electrode was used and functions as a quasi-reference electrode in that the potential of an AC electrode is stable.[30] The electrodes were not discharged below 2.5 V vs. Ca^{2+}/Ca to avoid possible conversion reactions or side reactions in the low voltage region. The thermodynamic potential of conversion reaction was calculated to be 2.58 V vs. Ca^{2+}/Ca based on the formation energies. Figure 2a shows the α-MoO_3 electrode delivered 236 and 165 mA h g^{-1} at a current density of 20 mA g^{-1} for the first discharge and charge capacity, respectively, with 83 mA h g^{-1} irreversible capacity in the first cycle which will be discussed later. This irreversible capacity is no longer observed after the first cycle.[31] α-MoO_3 electrode reversibly delivered a specific capacity of 165 mA h g^{-1} (discharge capacity basis), corresponding to 0.44 mol of Ca^{2+}/ MoO_3. The discharge-charge curves of the α-MoO_3 electrode show multiple plateaus suggesting the stepwise reactions, similar to previously observed behavior of α-MoO_3 in Li and Ca intercalation cases.[17,18,24,25] The specific capacity was centered around a 2.7 V vs. Ca^{2+}/Ca plateau. Some potential jump phenomena were observed in the first and second discharge curves, as previously seen in Zn intercalation into α-MoO_3[22], and they have been attributed to electrode phase transitions based on lattice layer shifts and/or cation re-ordering which takes some time to reach equilibrium.The multiple phase reactions are clearly seen in the dQ/dV curve with several cathodic and anodic peaks (Figure 2b). After the first cycle, the reduction peaks at 2.7, 2.8, and 3.1 V vs. Ca^{2+}/Ca and oxidations peaks at 2.8, 3, and 3.3 V vs. Ca^{2+}/Ca were shown, respectively, suggesting 3 redox peak pairs. The differences between each redox peak are 0.08, 0.18, and 0.18 V, indicating small voltage hysteresis. These values are significantly smaller when compared to the previously reported MoO_3 studies for CIB (Table S1). We suspect concentration polarization originating from limitations in diffusion was improved in moving to smaller particle sizes which leads to smaller voltage hysteresis. The α-MoO_3 electrode showed stable capacity retention and delivered a discharge capacity of 103 mA h g^{-1} after 200 cycles at 40 mA g^{-1} (Figure 2c). Furthermore, the Coulombic efficiency of the electrode stabilizes around 97.5 % through 200 cycles. The discharge-charge curves of the α-MoO_3 electrode for subsequent cycles during long-term cycling are presented in Figure S1. Based on the charge-discharge curves and data analysis, the reaction mechanism appears to remain consistent after 1st cycle once the t overpotential increase in the initial cycles is taken into account. Specific capacities of 163, 129, 102, 86 and 64 mA h g^{-1} (fifth discharge capacity at each current density) were achieved at 20, 40, 80, 120, and 200 mA g^{-1}, respectively (Figure 2d). When the rate returns to 200 mA g^{-1} from 20 mA g^{-1}, the discharge capacity recovered to 151 mA h g^{-1} (93% retention). The discharge-charge curves and the dQ/dV curves (Figure 2e and 2f) at high current densities still showed clear electrochemical reactions and the voltage hysteresis didn't increase significantly, indicating good reaction kinetics. The improved reaction kinetics can be attributed to small diffusion distances seen in the α-MoO_3 nanoparticles.[27,28] The results presented here are useful to consider molybdenum oxide host lattices as a possible CIB cathode system. The voltage difference (overpotential) between the charge/discharge potential and the quasi-equilibrium potential in Galvanostatic intermittent titration technique (GITT) is plotted in Figure S2c. It shows that the region where the potential jump phenomena appeared exhibited a larger polarization than the redox reaction of the main voltage plateau, suggesting that the energy barrier of redox reaction at higher voltage is higher than that of redox reaction at lower voltage. Even though direct comparison may not be suitable due to different particle sizes and different electrolytes, the overpotential was compared with that of α-MoO_3 in LIB[31] and the α-MoO_3 nanoparticles in a Ca cell showed a comparable or even smaller polarization, indicating the enhanced reaction kinetics.

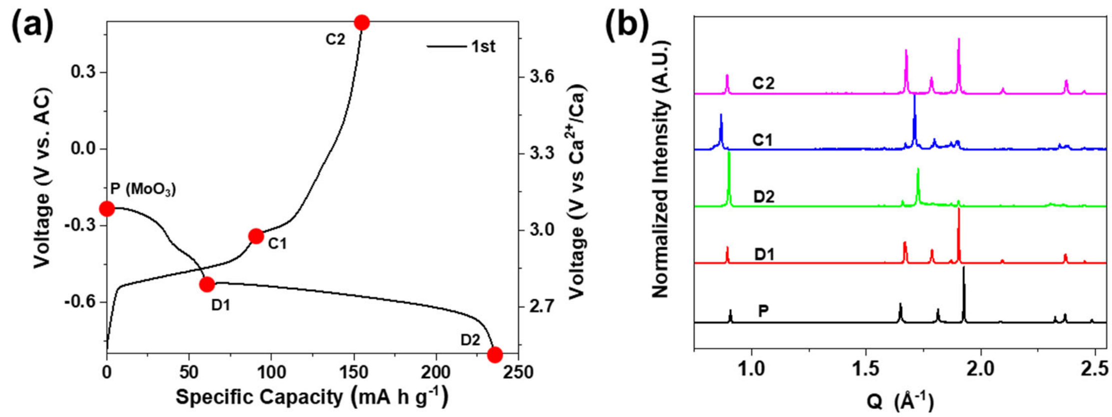

(c)

Charge State	a (Å)	b (Å)	c (Å)	α (°)	β (°)	γ (°)	V (Å^{-3})	Space Group
Pristine	3.96084(4)	13.8579(1)	3.69611(3)	90	90	90	202.876(4)	Pbnm
D1	3.90321(4)	14.0682(1)	3.73688(1)	90	90	90	205.197(3)	Cmcm
C2	3.89235(3)	14.0810(1)	3.73540(2)	90	90	90	204.732(3)	Cmcm

Figure 3. (a) Indication of various stages during the 1st cycle where ex situ sample was prepared. (b) Ex situ synchrotron XRD patterns of α-MoO_3 nanoparticles at four states of charge. (c) Cell parameters from Rietveld refinement and Pawley fitting results for α-MoO_3 nanoparticles at pristine, D1, and C2 states.

Ex situ XRD was performed with the electrodes discharged to D1 and D2 and charged back to C1 and C2 during the 1st cycle as marked on the charge-discharge curve (boundaries were made based on the respective redox reaction/plateau). These ex-situ samples were further used for other characterization studies after it was noted that α-MoO_3 showed a distinct phase transition during cycling (Figure 3b). Due to the difficulty in identifying the phase of D2 and C1 samples, Pawley fitting was only applicable for D1 and C2 samples. The pristine sample is a typical orthorhombic α-MoO_3 with a space group of *Pbnm* (62). Upon discharge, the symmetry of the orthorhombic lattice changes (Figure 3b) and the discharged D1 phase can be indexed with space group *Cmcm* (63). On further discharging, the formation of new phases can be seen in the high-resolution XRD of sample D2. The identification of new phases is challenging due to the complexity of reflections. However, a strong and sharp reflection is observed around 0.9 $Å^{-1}$, which is similar to the (020) reflection in the XRD of pristine and D1 samples. Since the (020) peaks correspond to the layering reflection in the stacking direction of MoO_6 layers, this new structure may result from the gliding of MoO_6 layers, which reduces the extent of ordering in the a/b direction. The phase transition from *Cmcm* phase to new structures is reversible. A trace amount of *Cmcm* phase can be observed in the charged sample C1. After further charging, the *Cmcm* phase is fully recovered as seen in the XRD data of sample C2. However, even charged up to 3.8 V vs. Ca^{2+}/Ca, the cathode is still not fully recovered to the pristine state. This is perhaps due to trapped inserted Ca^{+2} in the MoO_3 or the electrode underwent irreversible structural changes such as defect generation (anion loss), or layer rearrangement, accounting for irreversible capacity during the first cycle.[24] The unit cell parameters and volumes of P (pristine), D1, and C2 samples extracted from Rietveld refinements or Pawley fitting are summarized in Figure 3c. α-MoO_3 electrodes showed an irreversible structural change that doesn't seem to be related to a conversion reaction asany phase expected to be a product of the conversion reaction (Mo, MoO_2, CaO) was not identified while the high level of crystallinity of the host materials was maintained during the charge and discharge. Reaction mechanisms that are associated with a conversion reaction are typically accompanied with a loss in crystallinity. No significant volume expansion or morphology changes were observed during cycling indicating intercalation is the predominant reaction mechanism rather than a conversion reaction (Figure S4). The structure evolution after the first cycle was examined by ex situ XRD with twice cycled electrodes (Figure S5). It was confirmed that the first cycle irreversible structural change only occurred in the first cycle and that the phase transition after 1st cycle seems to have remained the same for the subsequent cycles which is in good agreement with discharge-charge curves of following cycles (Figure S1).

One thing to note is that (020) peak shifted toward higher q from D1 to D2 during discharge and shifted back toward lower q from D2 to C1 during charge. This change in d-spacing of the interlayer decreases with Ca insertion and increases with Ca de-insertion in the lower voltage plateau, which is contrary to typical intercalation behavior of other layered electrodes where a measurable expansion of the interlayer spacing was observed. However, this crystallographic behavior has previously been reported for α-MoO_3 in the low voltage region for Li intercalation cases, $Li_x[MoO_3]$ and appears to be associated with its complex intercalation mechanism.[15,32]

Figure S6b shows DFT-calculated structures of $Ca_1Mo_{36}O_{108}$ ($Ca_{0.03}MoO_3$) with a single Ca ion occupying various possible Ca sites and their formation energies. The $Ca_1Mo_{36}O_{108}$ composition was chosen for balancing the representation of the dilute Ca concentration and affordable simulation cell size. The formation energies for Ca intercalation into three symmetrically distinctive sites in α-MoO_3 are negative and the values are nearly constant over these Ca intercalation sites. Either Ca ion occupies the channel within the [MoO_6] octahedra layer in one of the sites (intralayer position), or Ca resides between MoO_6 layers in other two sites (interlayer position). For the interlayer positions, Ca sites are distinguished by different Ca-O coordination environments. As demonstrated by DFT calculation, the formation energies for Ca occupying inter- and intralayer positions are almost the same, which indicates that Ca can occupy both inter- and intralayer positions. Notably, Ca intercalation into the intralayer position can complicate the stacking order between Mo–O octahedra layers or affect the linkage of Mo–O octahedra layers.[15] In this case, d-spacing in the interlayer can decrease with Ca intercalation which happened from D1 to D2 during discharge and vice versa during charge.

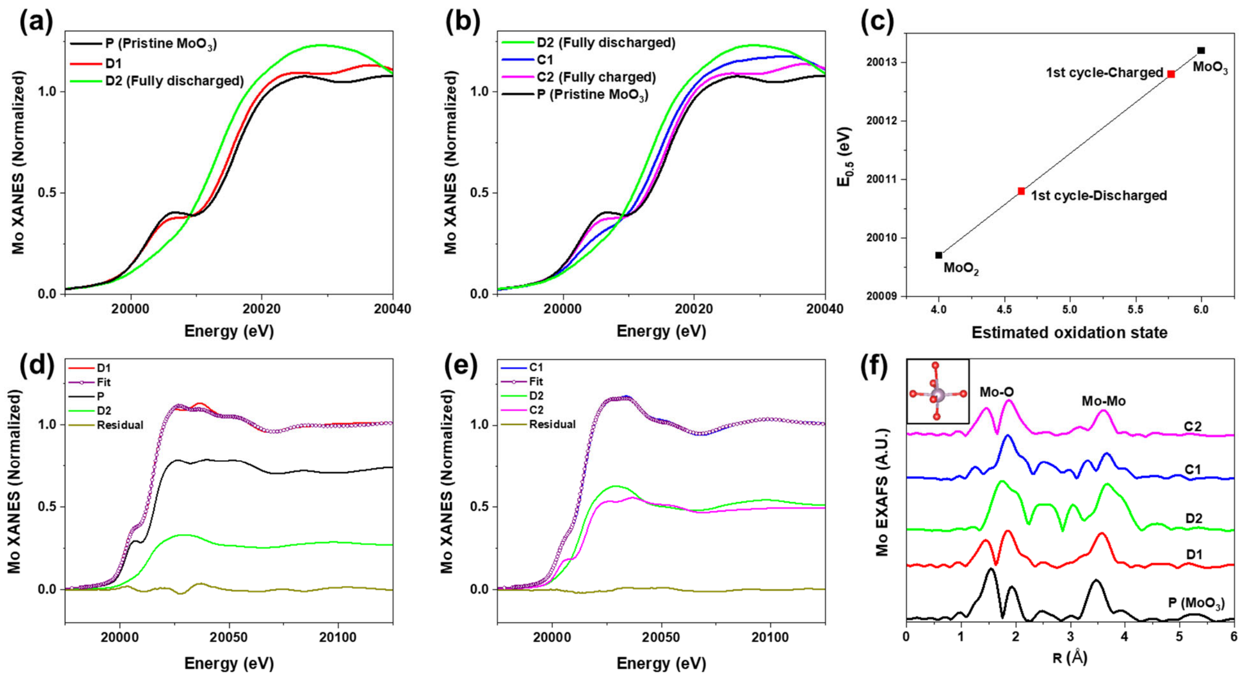

Figure 4. Ex situ Mo K-edge XANES spectra of α-MoO_3 nanoparticles at different states of charge during (a) discharge and (b) charge. (c) Estimation of oxidation state of Mo in α-MoO_3 nanoparticles before cycling and after discharge and charge using the Mo K-edge energy (at half height of normalized XANES spectra) shift. Linear combination fit for (d) D1 and (e) C1. Ex situ (f) Mo K-edge EXAFS spectra of α-MoO_3 at different states of charge (phase is not corrected). The inset shows a distorted MoO_6 octahedron of pristine of α-MoO_3.

Figure 4a and 4b show the Mo K-edge X-ray absorption near edge structure (XANES) spectra of α-MoO_3 at different charge states during cycling. A pre-edge peak is observed in pristine α-MoO_3 which is due to the transition from the 1s to 4d orbital.[33] The octahedral oxygen coordination is greatly distorted in α-MoO_3 because MoO_6 octahedron consists of four shorter Mo-O bonds and two much longer Mo-O bonds (the inset in Figure 4f). This induces the Mo s-d excitation, resulting in a pre-edge peak in Mo K-edge spectra. However, the intensity of the pre-edge peak decreases on discharge and disappears when the electrode is discharged to D2 state. This suggests that the Mo-O coordination environment is less distorted in Ca discharged α-MoO_3. The pre-edge peak reappeared during the charging process. The position of the main edge corresponding to a 1s → 5p transition is sensitive to the Mo oxidation state. The Mo K-edge shifted towards lower energies gradually due to the reduction of Mo^{6+} as the α-MoO_3 electrode is discharged. After charging, the Mo K-edge shifted back to higher energies, and the edge closely returns to the original position of α-MoO_3, indicating the reversible reduction and oxidation of Mo. The oxidation state of Mo in D2 and C2 states was estimated assuming the linear correlation between the edge energy and average oxidation state (Figure 4c).[34,35] The energy at half the height of normalized XANES spectra, was used to define the edge position. Based on this shift (Figure 4c) and the position of Mo^{4+} and Mo^{6+} standards, the Mo oxidation state in D2 and C2 states were determined to be roughly 4.6+ and 5.8+, respectively, indicating the electrochemical redox reaction contributes to the reversible capacity of α-MoO_3 mostly. A linear combination fit of XANES spectra of intermediate states was used for the estimation of the oxidation states of intermediate states during discharge and charge. The spectra of the D1 and C1 can be regarded as a linear combination of the end phases (discharged and charged states). The XANES spectra of D1 and C1 were fitted by using a linear combination of P/D2 and D2/C2, respectively (Figure 4d and 4e). According to the linear combination fit, D1 is composed of 73 % of P and 27 % of D2 and C1 is composed of 51 % of D2 and 49 % of C2 which is generally consistent with state of charges of D1 and C1 calculated based on electrochemical charge/discharge profiles. In the Fourier-transformed extended X-ray absorption fine structure (EXAFS) (Figure 4f), the peaks below 2 Å (phase is not corrected) can be assigned to Mo-O bonds and the peaks from 3 to 4 Å can be assigned to Mo-Mo interactions. The Mo-O peaks gradually merge during discharge. The amplitude increase for α-MoO_3 suggests that first neighboring oxygen atoms are rearranged and the noncentrosymmetric nature of the Mo-O environment is mitigated upon discharge which is consistent with the disappearance of a pre-edge peak in XANES. In D2 state, a new coordination shell just above 2 Å (2.5 Å phase-shifted) appears in the second and third shells. This could be due to scattering paths from calcium sites or a rearrangement of Mo upon deep Ca intercalation to a local coordination approaching a lower oxidation state of the Mo cations. The formation of shorter Mo-Mo interactions was previously reported for the case of Li intercalation into α-MoO_3.[36] After charging, the EXAFS spectrum of C2 was recovered and found to closely match the pristine (uncycled) sample, indicating good local structure reversibility.

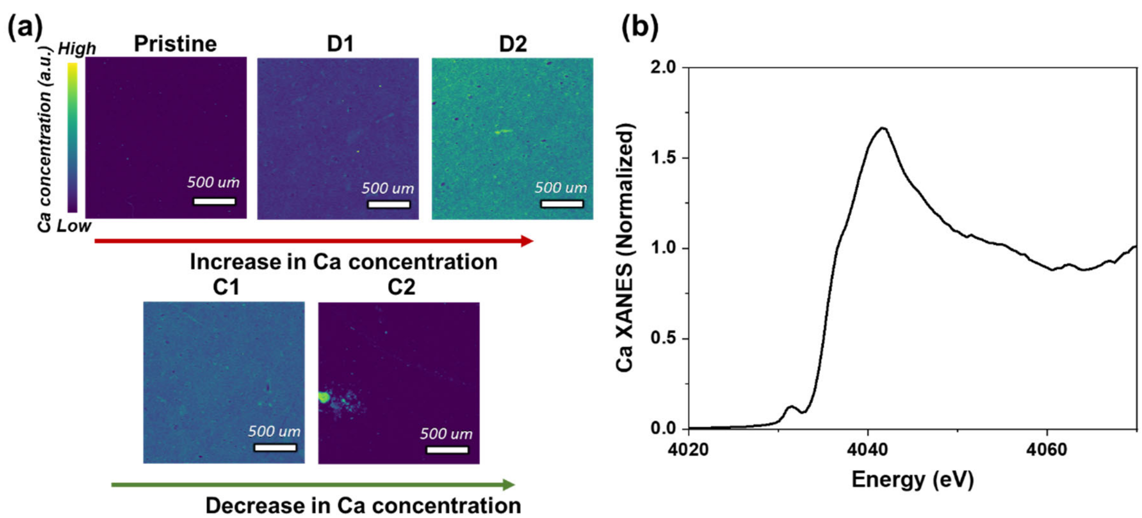

Figure 5. (a) XRF mapping of Ca in electrodes at different states of charge with an Incident beam energy of 4.3 keV. (b) Normalized Ca K-edge XANES spectrum measured from D2 (fully discharged).

Figure 5a shows Ca-ion concentration increases during discharge and decreases during charge as expected. The electrodes show a uniform Ca-ion distribution, indicating Ca-ion insertion and de-insertion occur homogeneously at the electrode level with the nanoparticle-based electrodes used for this study. The Ca K-edge XANES spectrum of D2 (fully discharged), which is highly sensitive to the local environment, is shown in Figure 5b.[37] The direct comparison between chemically calciated $Ca_{0.5}MoO_3$ and electrochemically prepared electrodes would be the most ideal, but unfortunately, it was not possible as we were unable to synthesize or acquire chemically calciated samples. Instead, the XANES spectrum of D2 was compared with electrolyte precipitate. A sample for electrolyte precipitate was prepared by dipping the electrode into the electrolyte and drying it (Figure S7). The spectrum from the electrode was different from that from electrolyte precipitate (i.e., $Ca(TFSI)_2$), where Ca exists on the surface. Also, a pre-edge peak was observed due to the transition from the 1s to 3d orbital which occurs when Ca is not in a centrosymmetric environment. This is opposite to the absence of pre-edge peak in Ca K-edge XANES spectrum of CaO[38], suggesting it is not a conversion reaction. The atomic ratio of Ca/Mo based on the Energy-dispersive X-ray spectroscopy (EDS) quantification results and calculated from discharge and charge capacity of EDS samples are shown in Table S2. It showed a similar tendency to the electrochemical capacity, however, much less Ca was detected from the fully charged samples, suggesting the irreversible capacity in the first cycle may not fully consist of Ca intercalation and may contain other contributions from side reactions, notably electrolyte decomposition. Based on the X-ray photoelectron spectroscopy (XPS) data (Figure S9), it was confirmed that a cathode electrolyte interphase layer was formed and that it mainly contained C-C, C-O, solvent decomposition products , and a Ca-O species. The data is consistent with the $TFSI^-$ salt itself being stable, as estimated from S 2p peak which is consistent with XRF data. We suspect that this electrolyte decomposition and formation of electrolyte interphase during discharge may contribute to relatively low coulombic efficiency.

In conclusion, α-MoO_3 as a practical Ca electrode material was re-examined using α-MoO_3 nanoparticles. α-MoO_3 nanoparticles were found to reversibly cycle Ca-ions and the electrode showed good long-term cyclability. Furthermore, the α-MoO_3 electrodes exhibited good rate performance and small hysteresis at high current density. The improved electrochemical performance of α-MoO_3 versus previously reported studies may be attributable to the enhanced reaction kinetics accessed by going to a nanoscale particle as it reduces the electron and ion diffusion lengths. Future work will seek to increase the specific capacity of α-MoO_3 will be focused on preparing low defect nanoparticles to improve active material utilization and higher capacitive capacity as well as addressing the role of size-dependent Ca storage mechanism in Mo-based oxides. This study suggests that resolving the rate limiting issues is an important step for the future design of multivalent batteries and investigating new electrode materials. The consistent changes in structure, electronic environment, and chemical composition were observed during cycling, indicating Ca can reversibly be inserted into and de-inserted from α-MoO_3. The main reaction mechanism appears to be an intercalation reaction that is initiated with an irreversible structural change in the first cycle. We believe this result shows a significant advance compared to previously reported oxide-based materials for CIBs and satisfies a significant milestone in the search for practical Ca batteries.

ASSOCIATED CONTENT

Supporting Information

The Supporting Information is available free of charge at

Galvanostatic discharge-charge curves of subsequent cycles, GITT curves, Pawley fitting of ex situ α-MoO_3 electrodes, Ex situ SEM images of α-MoO_3 nanoparticles, Ex situ synchrotron XRD patterns of 2^{nd} cycled samples, Various possible Ca sites predicted by DFT calculations, XRF mapping of Ca in a control sample and corresponding normalized Ca K-edge XANES spectrum, Differential capacity plots for delithiation of $LiFePO_4$ in different types of cells, XPS analysis for α-MoO_3 electrodes, Voltage hysteresis comparison among previously reported MoO_3 based Ca cathodes and the present work, Ex situ EDS results for α-MoO_3 electrodes.

AUTHOR INFORMATION

Corresponding Author

* E-mail: vaughey@anl.gov

Notes

The authors declare no competing financial interest.

ACKNOWLEDGMENT

This work was supported by the Joint Center for Energy Storage Research, an Energy Innovation Hub funded by the U.S. Department of Energy, Office of Science, Basic Energy Sciences. This research used resources of the Advanced Photon Source, a U.S. Department of Energy (DOE) Office of Science User Facility operated for the DOE Office of Science by Argonne National Laboratory under Contract No. DE-AC02-06CH11357. This work is conducted at Argonne National Laboratory supported by the U.S. Department of Energy under contract DE-A02-06CH11357. Use of the Center for Nanoscale Materials, an Office of Science user facility, was supported by the U.S. Department of Energy, Office of Science, Office of Basic Energy Sciences, under Contract No. DE-AC02-06CH11357. The XAS research used beamline 8-BM (TES) of the National Synchrotron Light Source II, a U.S. Department of Energy (DOE) Office of Science User Facility operated for the DOE Office of Science by Brookhaven National Laboratory under Contract No. DE-SC0012704.

REFERENCES

(1) Etacheri, V.; Marom, R.; Elazari, R.; Salitra, G.; Aurbach, D. Challenges in the development of advanced Li-ion batteries: a review. *Energy Environ. Sci*. **2011,** *4,* 3243−3262.

(2) Blomgren, G. E. The Development and Future of Lithium Ion Batteries. *J. Electrochem. Soc.* **2016,** *164*, A5019−A5025.

(3) Ponrouch, A.; Bitenc, J.; Dominko, R.; Lindahl, N.; Johansson, P.; Palacin, M. R. Multivalent rechargeable batteries. *Energy Storage Mater.* **2019,** *20*, 253−262.

(4) Canepa, P.; Sai Gautam, G.; Hannah, D. C.; Malik, R.; Liu, M.; Gallagher, K. G.; Persson, K. A.; Ceder, G. Odyssey of Multivalent Cathode Materials: Open Questions and Future Challenges. *Chem. Rev.* **2017,** *117*, 4287−4341.

(5) Liu, M.; Rong, Z.; Malik, R.; Canepa, P.; Jain, A.; Ceder, G.; Persson, K. A. Spinel compounds as multivalent battery cathodes: a systematic evaluation based on ab initio calculations. *Energy Environ. Sci*. **2015,** *8*, 964−974.

(6) Ponrouch, A.; Palacin, M. R. On the road toward calcium-based batteries. *Curr. Opin. Electrochem.* **2018,** *9*, 1−7.

(7) Gummow, R. J.; Vamvounis, G.; Kannan, M. B.; He, Y. Calcium-Ion Batteries: Current State-of-the-Art and Future Perspectives. *Adv. Mater.* **2018,** *30*, e1801702.

(8) Wang, D.; Gao, X.; Chen, Y.; Jin, L.; Kuss, C.; Bruce, P. G. Plating and stripping calcium in an organic electrolyte. *Nat. Mater.* **2018,** *17*, 16−20.

(9) Ponrouch, A.; Frontera, C.; Barde, F.; Palacin, M. R. Towards a calcium-based rechargeable battery. *Nat. Mater.* **2016,** *15*, 169−72.

(10) Li, Z.; Fuhr, O.; Fichtner, M.; Zhao-Karger, Z. Towards stable and efficient electrolytes for room-temperature rechargeable calcium batteries. *Energy Environ. Sci*. **2019,** *12*, 3496−3501.

(11) Shyamsunder, A.; Blanc, L. E.; Assoud, A.; Nazar, L. F. Reversible Calcium Plating and Stripping at Room Temperature Using a Borate Salt. *ACS Energy Lett.* **2019,** *4*, 2271−2276.

(12) Jie, Y.; Tan, Y.; Li, L.; Han, Y.; Xu, S.; Zhao, Z.; Cao, R.; Ren, X.; Huang, F.; Lei, Z.; Tao, G.; Zhang, G.; Jiao, S., Electrolyte Solvation Manipulation Enables Unprecedented Room-Temperature Calcium-Metal Batteries. *Angew. Chem., Int. Ed.* **2020,** *59*, 12689−12693.

(13) Su, Z.; Ren, W.; Guo, H.; Peng, X.; Chen, X.; Zhao, C., Ultrahigh Areal Capacity Hydrogen-Ion Batteries with MoO_3 Loading Over 90 mg cm^{-2}. *Adv. Funct. Mater.* **2020,** *30*, 2005477.

(14) Wang, X.; Xie, Y.; Tang, K.; Wang, C.; Yan, C., Redox Chemistry of Molybdenum Trioxide for Ultrafast Hydrogen-Ion Storage. *Angew. Chem., Int. Ed.* **2018,** *57* , 11569-11573.

(15) Tsumura, T.; Inagaki, M. Lithium insertion/extraction reaction on crystalline MoO_3. *Solid State Ionics* **1997**, *104*, 183−189.

(16) Hashem, A. M.; Askar, M. H.; Winter, M.; Albering, J. H.; Besenhard, J. O., Two-phase reaction mechanism during chemical lithium insertion into α-MoO_3. *Ionics* **2007,** *13*, 3−8.

(17) Mai, L. Q.; Hu, B.; Chen, W.; Qi, Y. Y.; Lao, C. S.; Yang, R. S.; Dai, Y.; Wang, Z. L., Lithiated MoO_3 Nanobelts with Greatly Improved Performance for Lithium Batteries. *Adv. Mater.* **2007,** *19*, 3712−3716.

(18) Hashem, A. M.; Groult, H.; Mauger, A.; Zaghib, K.; Julien, C. M., Electrochemical properties of nanofibers α-MoO_3 as cathode materials for Li batteries. *J. Power Sources* **2012,** *219*, 126−132.

(19) Zhou, L.; Yang, L.; Yuan, P.; Zou, J.; Wu, Y.; Yu, C. r-MoO_3 Nanobelts: A High Performance Cathode Material for Lithium Ion Batteries *J. Phys. Chem. C* **2010**, *114*, 21868−21872.

(20) Gershinsky, G.; Yoo, H. D.; Gofer, Y.; Aurbach, D., Electrochemical and spectroscopic analysis of Mg^{2+} intercalation into thin film electrodes of layered oxides: V_2O_5 and MoO_3. *Langmuir* **2013,** *29*, 10964−10972.

(21) Xiong, T.; Zhang, Y.; Wang, Y.; Lee, W. S. V.; Xue, J., Hexagonal MoO_3 as a zinc intercalation anode towards zinc metal-free zinc-ion batteries. *J. Mater. Chem. A* **2020,** *8*, 9006−9012.

(22) Liu, Y.; Wang, J.; Zeng, Y.; Liu, J.; Liu, X.; Lu, X., Interfacial Engineering Coupled Valence Tuning of MoO_3 Cathode for High-Capacity and High-Rate Fiber-Shaped Zinc-Ion Batteries. *Small* **2020,** *16*, e1907458.

(23) He, X.; Zhang, H.; Zhao, X.; Zhang, P.; Chen, M.; Zheng, Z.; Han, Z.; Zhu, T.; Tong, Y.; Lu, X., Stabilized Molybdenum Trioxide Nanowires as Novel Ultrahigh-Capacity Cathode for Rechargeable Zinc Ion Battery. *Adv. Sci.* **2019,** *6*, 1900151.

(24) Cabello, M.; Nacimiento, F.; Alcántara, R.; Lavela, P.; Pérez Vicente, C.; Tirado, J. L. Applicability of Molybdite as an Electrode Material in Calcium Batteries: A Structural Study of Layer-type Ca_xMoO_3. *Chem. Mater.* **2018,** *30*, 5853−5861.

(25) Tojo, T.; Tawa, H.; Oshida, N.; Inada, R.; Sakurai, Y., Electrochemical characterization of a layered α-MoO_3 as a new cathode material for calcium ion batteries. *J. Electroanal. Chem.* **2018,** *825*, 51−56.

(26.) Hannah, D. C.; Sai Gautam, G.; Canepa, P.; Ceder, G., On the Balance of Intercalation and Conversion Reactions in Battery Cathodes. *Adv. Energy Mater.* **2018,** *8* 1800379.

(27) Blanc, L. E.; Sun, X.; Shyamsunder, A.; Duffort, V.; Nazar, L. F., Direct Nano-Synthesis Methods Notably Benefit Mg-Battery Cathode Performance. *Small Methods* **2020,** 2000029.

(28) Chen, W.; Zhan, X.; Luo, B.; Ou, Z.; Shih, P. C.; Yao, L.; Pidaparthy, S.; Patra, A.; An, H.; Braun, P. V.; Stephens, R. M.; Yang, H.; Zuo, J. M.; Chen, Q., Effects of Particle Size on Mg^{2+} Ion Intercalation into λ-MnO_2 Cathode Materials. *Nano Lett*. **2019**, *19*, 4712−4720.

(29) Chae, M. S.; Kwak, H. H.; Hong, S.-T., Calcium Molybdenum Bronze as a Stable High-Capacity Cathode Material for Calcium-Ion Batteries. *ACS Appl. Energy Mater.* **2020,** *3*, 5107−5112.

(30) Kim, S.; Yin, L.; Lee, M. H.; Parajuli, P.; Blanc, L.; Fister, T. T.; Park, H.; Kwon, B. J.; Ingram, B. J.; Zapol, P.; Klie, R. F.; Kang, K.; Nazar, L. F.; Lapidus, S. H.; Vaughey, J. T. High-Voltage Phosphate Cathodes for Rechargeable Ca-Ion Batteries. *ACS Energy Lett*. **2020**, *5*, 3203−3211.

(31) Wustrow, A.; Hancock, J. C.; Incorvati, J. T.; Vaughey, J. T.; Poeppelmeier, K. R., Effect of Fluoride Doping on Lithium Diffusivity in Layered Molybdenum Oxide. *ACS Appl. Energy Mater.* **2019,** *2*, 2080−2086.

(32) Besenhard, J. O.; Heydecke, J.; Fritz, H. P. Characteristics of molybdenum oxide and chromium oxide cathodes in primary and secondary organic electrolyte lithium batteries. I. Morphology, structure and their changes during discharge and cycling. *Solid State Ionics* **1982**, *6*, 215−224.

(33) Gaillard, C.; Chevarier, N.; Den Auwer, C.; Millard-Pinard, N.; Delichere, P.; Sainsot, P. Study of mechanisms involved in thermal migration of molybdenum and rhenium in apatites. *J. Nucl. Mater.* **2001**, *299*, 43−52.

(34) Wen, B.; Chernova, N. A.; Zhang, R.; Wang, Q.; Omenya, F.; Fang, J.; Whittingham, M. S., Layered Molybdenum (Oxy)Pyrophosphate as Cathode for Lithium-Ion Batteries. *Chem. Mater.* **2013,** *25*, 3513−3521.

(35) Bak, S.-M.; Qiao, R.; Yang, W.; Lee, S.; Yu, X.; Anasori, B.; Lee, H.; Gogotsi, Y.; Yang, X.-Q., Na-Ion Intercalation and Charge Storage Mechanism in 2D Vanadium Carbide. *Adv. Energy Mater.* **2017,** *7,* 1700959.

(36) Kang, J.-H.; Paek, S.-M.; Choy, J.-H., In Situ X-ray Absorption Spectroscopic Study for α-MoO_3 Electrode upon Discharge/Charge Reaction in Lithium Secondary Batteries. *Bull. Korean Chem. Soc.* **2010,** *31*, 3675−3678.

(37) Sowrey, F. E.; Skipper, L. J.; Pickup, D. M.; Drake, K. O.; Lin, Z.; Smith, M. E.; Newport, R. J., Systematic empirical analysis of calcium–oxygen coordination environment by calcium K-edge XANES. *Phys. Chem. Chem. Phys.* **2004,** *6*, 188−192.

(38) Rodriguez, J. A.; Wang, X. Q.; Hanson, J. C.; Liu, G.; Iglesias-Juez, A.; Fernandez-Garcia, M., The behavior of mixed-metal oxides: Structural and electronic properties of $Ce_{1-x}Ca_xO_2$ and $Ce_{1-x}Ca_xO_{2-x}$. *J. Chem. Phys.* **2003**, *119*, 5659−5669.

TOC Graphic:

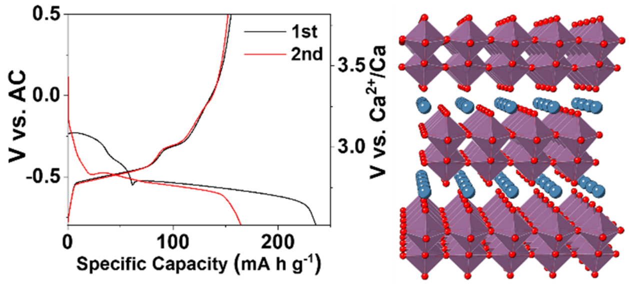

0.5
0.0
-0.5
V vs. AC
1st
2nd
3.5
3.0
V vs. Ca2+/Ca
0
100
200
Specific Capacity (mA h g-1)